RESONANCES IN $\Lambda_c^+ \to pK^-\pi^+$ DECAYS

AND

Λ_c^+ POLARIZATION

MILIND V. PUROHIT
E791
UNIV. OF S. CAROLINA

The E-791 Collaboration

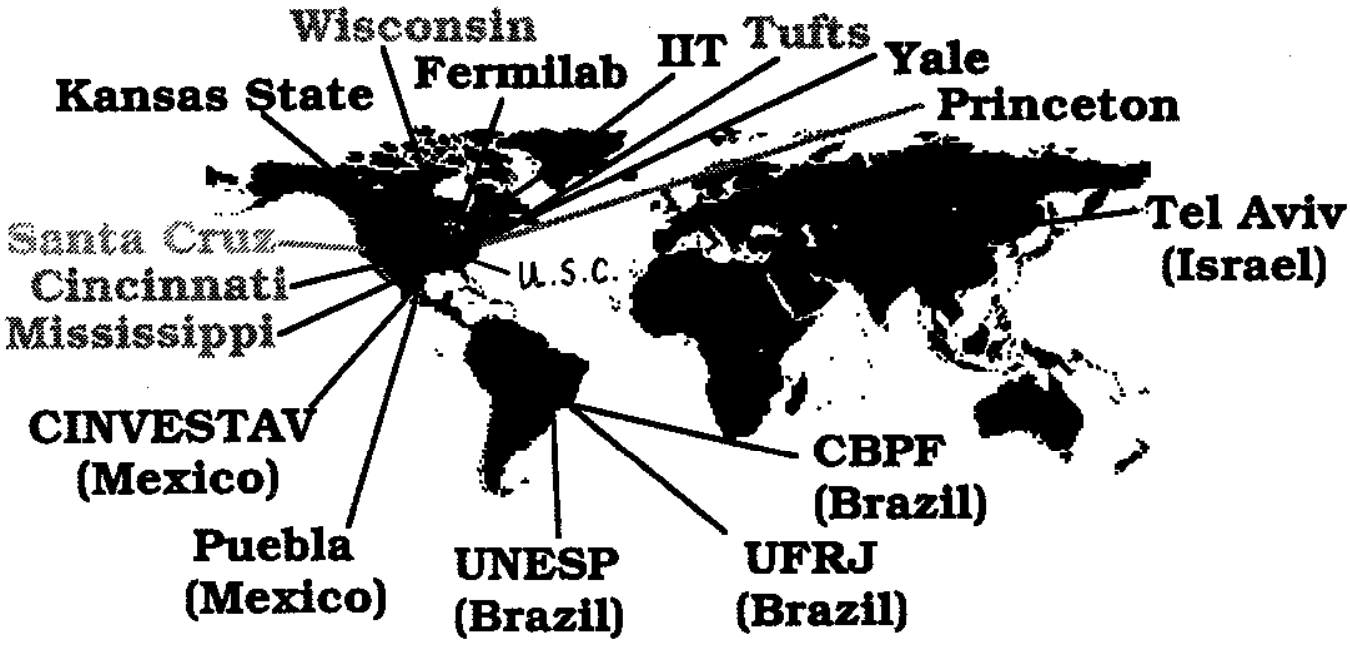

Centro Brasileiro de Pesquisas Fisicas (CBPF)
University of California - Santa Cruz
University of Cincinnati
Fermilab
Illinois Institute of Technology (IIT)
Kansas State University
CINVESTAV (Mexico)
University of Mississippi
Princeton University
Universidad Autonoma de Puebla
Universidade Federal do Rio de Janeiro (UFRJ)
UNESP - Sao Jose do Rio Preto
Tel Aviv University
Tufts University
University of Wisconsin - Madison
Yale University
University of South Carolina

E791

- 500 GeV π^- beam incident on Pt, Diamond foils
- Produced and recorded 20 billion events

- Fixed target spectrometer featuring Silicon strip detectors in the beam and after the target
  - Magnetic spectrometer with PWC's and DC's.
  - EM, Hadronic calorimeter
  - Muon wall

- Charm decays detected by vertex separation

- Physics includes DDbar mixing, CP violation studies, searches for FCNC, form factors, BRs, production, charm baryon resonances ...

E-791 Spectrometer

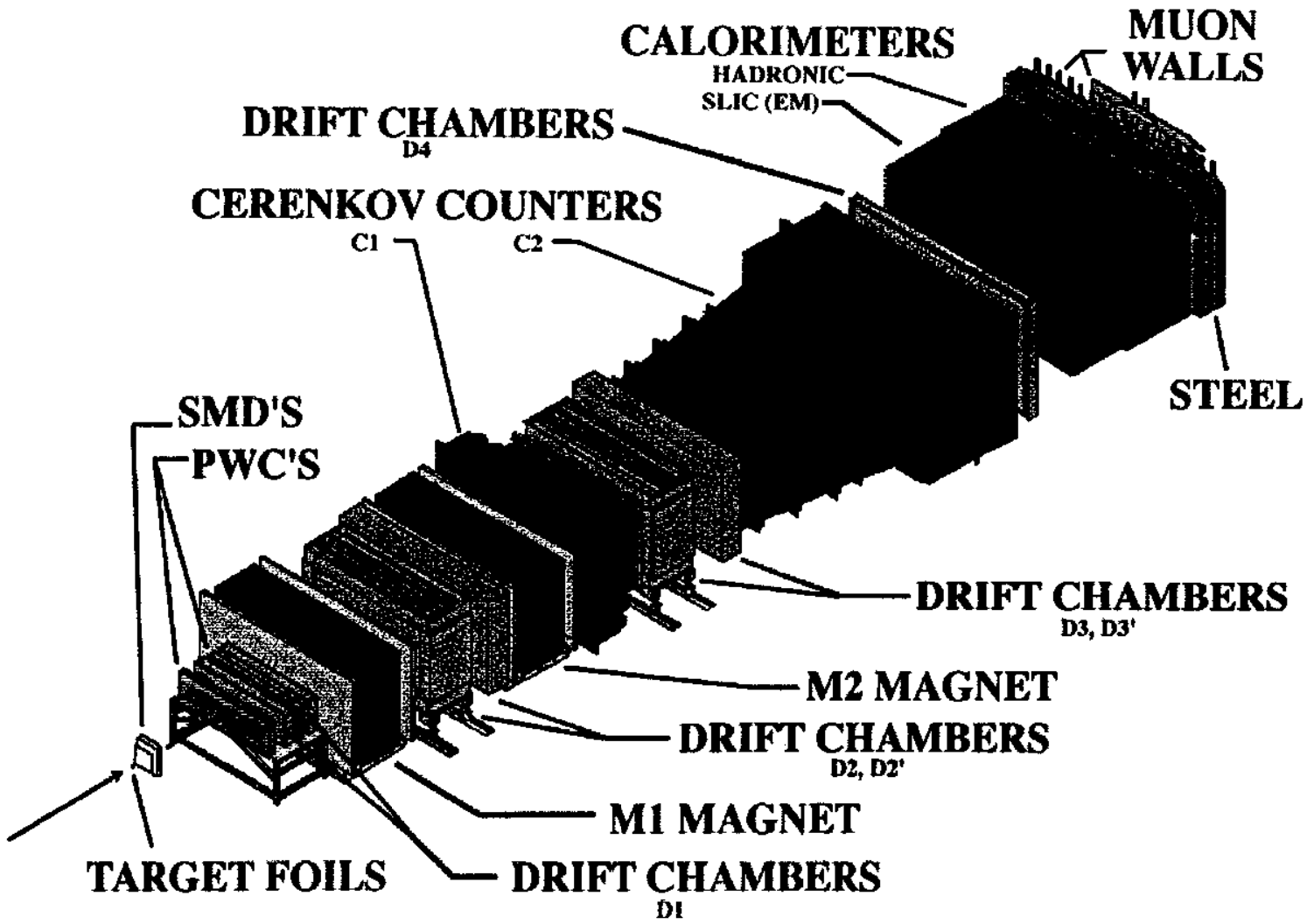

$\Lambda_c^+ \to p K^- \pi^+$

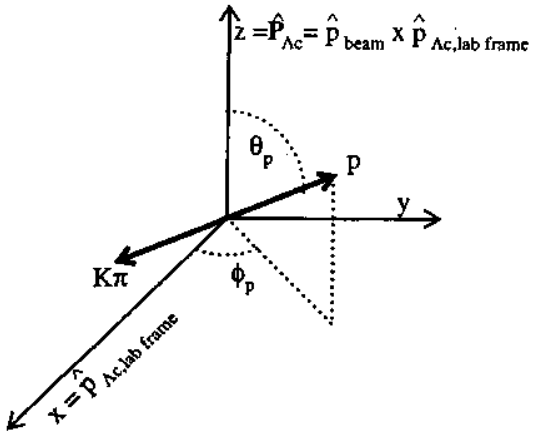

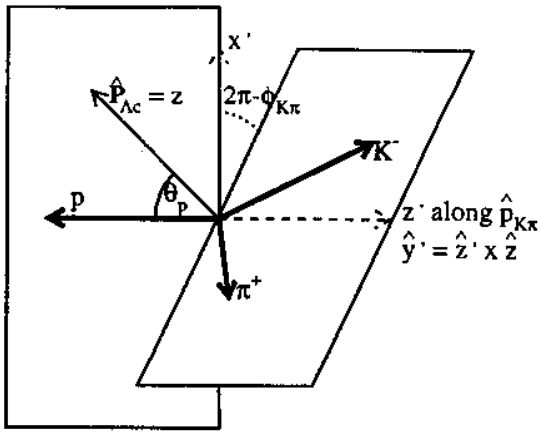

Spectator

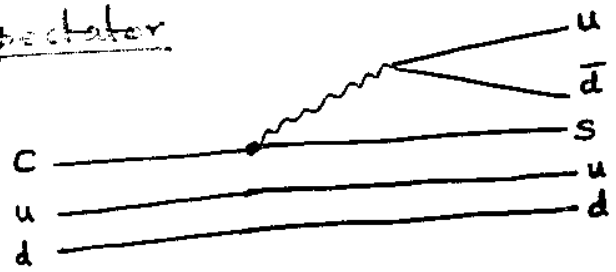

e.g., $p\bar{K}^{*0}$

Exchange

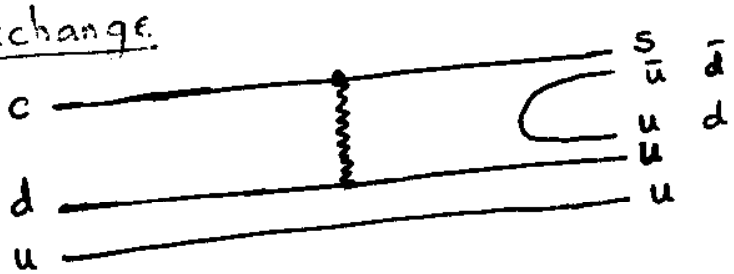

e.g., $p\overline{K^{*0}}$, $\Delta^{++} K^-$

charm baryon decay rates. The most direct components of the $\Lambda_c^+ \to pK^-\pi^+$ decays (and charge conjugate decays which are implied throughout this paper) include the nonresonant $pK^-\pi^+$ decay, and the $p\overline{K}^{*0}(890)$ and $\Lambda(1520)\pi^+$ two-body decays. All three of these decays can be described by spectator and W-exchange amplitudes. In lowest order, the $\Delta^{++}(1232)K^-$ decay can occur only via the exchange amplitude. Exchange amplitudes are suppressed in charm meson decays, at least at the quark level, because of helicity and form-factor effects. These effects are not expected to inhibit exchange amplitudes for charm baryons due to the three-body nature of the interaction. To understand fully this system of decays, as well as other charmed baryon decays, a complete resonant amplitude analysis is needed.

The charm baryon and its decay products carry spin and the charm baryon may be polarized upon production. Previous charm pseudoscalar meson decay analyses have studied structure in the two-dimensional space of the decay product effective masses (Dalitz plot distributions), but the spin effects just described require five kinematic variables for a complete description. While this complicates the analysis, it affords greater sensitivity to the parameters of interest. As a by-product of the analysis, the production polarization of the Λ_c^+, $\mathbf{P}_{\Lambda_c}$, is also measured. This analysis is the first five dimensional amplitude analysis and, as such, is unique.

2 Formalism

We parameterize the observed decay rate as a function of the Λ_c^+ polarization, $\mathbf{P}_{\Lambda_c}$, and of the amplitudes and relative phases of each intermediate two-body resonance decay. We assume that the nonresonant decay is described by an amplitude that is constant across phase space. The differential decay rate $d\Gamma$ (or signal density S) may be expressed as

$$\begin{aligned} d\Gamma \sim S(\vec{x}) = & \frac{(1+\mathbf{P}_{\Lambda_c})}{2}\left(\left|\sum_r B_r(m_r)\alpha_{r,\frac{1}{2},\frac{1}{2}}\right|^2 + \left|\sum_r B_r(m_r)\alpha_{r,\frac{1}{2},-\frac{1}{2}}\right|^2\right) \\ & + \frac{(1-\mathbf{P}_{\Lambda_c})}{2}\left(\left|\sum_r B_r(m_r)\alpha_{r,-\frac{1}{2},\frac{1}{2}}\right|^2 + \left|\sum_r B_r(m_r)\alpha_{r,-\frac{1}{2},-\frac{1}{2}}\right|^2\right) \quad (1) \end{aligned}$$

where α_{r,m,λ_p} is the complex decay amplitude for resonance r given m, the spin projection of the Λ_c on the z-axis, and λ_p, the proton helicity in the Λ_c rest frame.

$B_r(m_r)$ in Equation 1 is the normalized relativistic Breit-Wigner amplitude

corrected for the centrifugal barrier[3]. Given the decay mode $\Lambda_c \to r(\to ab)c$,

$$B_r(m_r) = (-2|p_c||p_a|)^L \frac{F_{\Lambda_c} F_r}{m_0^2 - m_r^2 - i m_0 \Gamma_r} \tag{2}$$

where

$$\Gamma_r = \Gamma_0 (\frac{q}{q_0})^{2L+1} \frac{m_0}{m_r} \frac{F_r^2(q)}{F_r^2(q_0)} \tag{3}$$

for resonance r at the reconstructed two body mass m_r, with the momentum q (and q_0 when $m_r = m_0$) of a daughter particle in the resonance's rest frame, and with resonance mass and width m_0 and Γ_0 as found in [2]. Using this convention, we set $B_r(m_r)$ for the nonresonant decay to be 1.0. F_L is the strong coupling factor at the appropriate decay vertex, and is in the Blatt-Weisskopf form as described in table 1 below. Table 2 lists the range of the strong interaction, R_X.

Table 1
We list here the expressions for F and values of R used in the Breit-Wigner amplitude.

L	F_L
0	1
1	$(1 + R_X^2 q^2)^{-1/2}$
2	$(9 + 3R_X^2 q^2 + R_X^4 q^4)^{-1/2}$

Table 2
We list here the expressions for F and values of R used in the Breit-Wigner amplitude.

X	R_X $(\mathrm{GeV/c^2})^{-1}$
$\overline{K}^{*0}(890)$	3.4 [4]
$\Delta^{++}(1232)$	5.22 [5]
$\Lambda(1520)$	6.29 [6]
Λ_c^+	5.07 [7]

In Tables 3–6, where the amplitudes α_{r,m,λ_p} (derived using the helicity formalism described in [8]) can be seen more explicitly, the direction (ϕ_r, θ_r) is the

direction of the resonance, r, in the Λ_c rest frame, using the convention of [9]. The primed angles refer to the direction of one of the resonance's daughters in the resonance's rest frame.

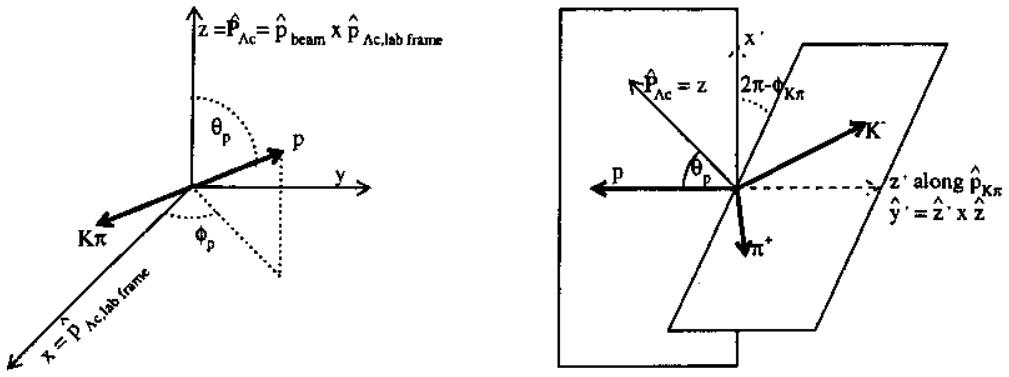

Fig. 1. Definition of angles used in analysis using $\Lambda_c^+ \to p\overline{K^{*0}} \to pK^-\pi^+$ as an example. In both figures the Λ_c^+ is at rest. In the first figure, which defines (θ_p, ϕ_p), the x-axis is along the direction of motion of the Λ_c^+ in the lab frame and the z-axis is the polarization axis, normal to the plane of production. In the second figure we define $\phi_{K\pi}$ which is the angle between the plane containing the $\overline{K^{*0}}$ decay products and the plane containing the proton and the x-axis.

Note that the decay amplitudes for each resonance have contributions to each of the four terms. Each event in the final data sample is described by five kinematic variables of interest (two two-body masses and the decay angles θ_p, ϕ_p, and $\phi_{K\pi}$ as defined in Figure 1) which are determined after the $pK\pi$ reconstructed mass is constrained to the Λ_c mass. We chose the quantization axis (the z-axis in the Λ_c rest frame) to be normal to the Λ_c production plane (as defined by $\hat{p}_{\rm beam} \times \hat{p}_{\Lambda_c}$, where $\hat{p}_{\rm beam}$ is the beam direction and $\hat{p}_{\Lambda_c}$ is the Λ_c production direction in the lab frame). The x-axis in the Λ_c rest frame is chosen to be the direction of the Λ_c in the lab frame.

Table 3
Amplitudes for $\Lambda_c^+(\frac{1}{2}^+) \to (\overline{K}^{*0}(890)(1^-) \to K^-\pi^+)p(\frac{1}{2}^+)$ decay mode.

m	λ_p	Amplitude
$\frac{1}{2}$	$\frac{1}{2}$	$E_1 e^{i\phi_{E_1}} \, d^{\frac{1}{2}}_{\frac{1}{2}\frac{1}{2}}(\theta_{\overline{K}^{*0}}) \, d^1_{10}(\theta'_K) e^{i\phi'_K} + E_2 e^{i\phi_{E_2}} \, d^{\frac{1}{2}}_{\frac{1}{2}-\frac{1}{2}}(\theta_{\overline{K}^{*0}}) \, d^1_{00}(\theta'_K) e^{i\phi_{\overline{K}^{*0}}}$
$\frac{1}{2}$	$-\frac{1}{2}$	$E_3 e^{i\phi_{E_3}} \, d^{\frac{1}{2}}_{\frac{1}{2}\frac{1}{2}}(\theta_{\overline{K}^{*0}}) \, d^1_{00}(\theta'_K) + E_4 e^{i\phi_{E_4}} \, d^{\frac{1}{2}}_{\frac{1}{2}-\frac{1}{2}}(\theta_{\overline{K}^{*0}}) \, d^1_{-10}(\theta'_K) e^{i(\phi_{\overline{K}^{*0}} - \phi'_K)}$
$-\frac{1}{2}$	$\frac{1}{2}$	$E_1 e^{i\phi_{E_1}} \, d^{\frac{1}{2}}_{-\frac{1}{2}\frac{1}{2}}(\theta_{\overline{K}^{*0}}) \, d^1_{10}(\theta'_K) e^{-i(\phi_{\overline{K}^{*0}} - \phi'_K)} + E_2 e^{i\phi_{E_2}} \, d^{\frac{1}{2}}_{-\frac{1}{2}-\frac{1}{2}}(\theta_{\overline{K}^{*0}}) \, d^1_{00}(\theta'_K)$
$-\frac{1}{2}$	$-\frac{1}{2}$	$E_3 e^{i\phi_{E_3}} \, d^{\frac{1}{2}}_{-\frac{1}{2}\frac{1}{2}}(\theta_{\overline{K}^{*0}}) \, d^1_{00}(\theta'_K) e^{-i\phi_{\overline{K}^{*0}}} + E_4 e^{i\phi_{E_4}} \, d^{\frac{1}{2}}_{-\frac{1}{2}-\frac{1}{2}}(\theta_{\overline{K}^{*0}}) \, d^1_{-10}(\theta'_K) e^{-i\phi'_K}$

Table 4
Amplitudes for $\Lambda_c^+(\frac{1}{2}^+) \to (\Delta^{++}(1232)(\frac{3}{2}^+) \to p\pi^+)K^-$ decay mode.

m	λ_p	Amplitude
$\frac{1}{2}$	$\frac{1}{2}$	$F_1 e^{i\phi_{F_1}} d^{\frac{1}{2}}_{\frac{1}{2}\frac{1}{2}}(\theta_{\Delta++}) d^{\frac{3}{2}}_{\frac{1}{2}\frac{1}{2}}(\theta'_p) + F_2 e^{i\phi_{F_2}} d^{\frac{1}{2}}_{\frac{1}{2}-\frac{1}{2}}(\theta_{\Delta++}) d^{\frac{3}{2}}_{-\frac{1}{2}\frac{1}{2}}(\theta'_p) e^{i(\phi_{\Delta++}-\phi'_p)}$
$\frac{1}{2}$	$-\frac{1}{2}$	$F_1 e^{i\phi_{F_1}} d^{\frac{1}{2}}_{\frac{1}{2}\frac{1}{2}}(\theta_{\Delta++}) d^{\frac{3}{2}}_{\frac{1}{2}-\frac{1}{2}}(\theta'_p) e^{i\phi'_p} + F_2 e^{i\phi_{F_2}} d^{\frac{1}{2}}_{\frac{1}{2}-\frac{1}{2}}(\theta_{\Delta++}) d^{\frac{3}{2}}_{-\frac{1}{2}-\frac{1}{2}}(\theta'_p) e^{i\phi_{\Delta++}}$
$-\frac{1}{2}$	$\frac{1}{2}$	$F_1 e^{i\phi_{F_1}} d^{\frac{1}{2}}_{-\frac{1}{2}\frac{1}{2}}(\theta_{\Delta++}) d^{\frac{3}{2}}_{\frac{1}{2}\frac{1}{2}}(\theta'_p) e^{-i\phi_{\Delta++}} + F_2 e^{i\phi_{F_2}} d^{\frac{1}{2}}_{-\frac{1}{2}-\frac{1}{2}}(\theta_{\Delta++}) d^{\frac{3}{2}}_{-\frac{1}{2}\frac{1}{2}}(\theta'_p) e^{-i\phi'_p}$
$-\frac{1}{2}$	$-\frac{1}{2}$	$F_1 e^{i\phi_{F_1}} d^{\frac{1}{2}}_{-\frac{1}{2}\frac{1}{2}}(\theta_{\Delta++}) d^{\frac{3}{2}}_{\frac{1}{2}-\frac{1}{2}}(\theta'_p) e^{-i(\phi_{\Delta++}-\phi'_p)} + F_2 e^{i\phi_{F_2}} d^{\frac{1}{2}}_{-\frac{1}{2}-\frac{1}{2}}(\theta_{\Delta++}) d^{\frac{3}{2}}_{-\frac{1}{2}-\frac{1}{2}}(\theta'_p)$

Table 5
Amplitudes for $\Lambda_c^+(\frac{1}{2}^+) \to (\Lambda(1520)(\frac{3}{2}^-) \to pK^-)\pi^+$ decay mode.

m	λ_p	Amplitude
$\frac{1}{2}$	$\frac{1}{2}$	$H_1 e^{i\phi_{H_1}} d^{\frac{1}{2}}_{\frac{1}{2}\frac{1}{2}}(\theta_{\Lambda(1520)}) d^{\frac{3}{2}}_{\frac{1}{2}\frac{1}{2}}(\theta'_p) + H_2 e^{i\phi_{H_2}} d^{\frac{1}{2}}_{\frac{1}{2}-\frac{1}{2}}(\theta_{\Lambda(1520)}) d^{\frac{3}{2}}_{-\frac{1}{2}\frac{1}{2}}(\theta'_p) e^{i(\phi_{\Lambda(1520)}-\phi'_p)}$
$\frac{1}{2}$	$-\frac{1}{2}$	$-(H_1 e^{i\phi_{H_1}} d^{\frac{1}{2}}_{\frac{1}{2}\frac{1}{2}}(\theta_{\Lambda(1520)}) d^{\frac{3}{2}}_{\frac{1}{2}-\frac{1}{2}}(\theta'_p) e^{i\phi'_p} + H_2 e^{i\phi_{H_2}} d^{\frac{1}{2}}_{\frac{1}{2}-\frac{1}{2}}(\theta_{\Lambda(1520)}) d^{\frac{3}{2}}_{-\frac{1}{2}-\frac{1}{2}}(\theta'_p) e^{i\phi_{\Lambda(1520)}})$
$-\frac{1}{2}$	$\frac{1}{2}$	$H_1 e^{i\phi_{H_1}} d^{\frac{1}{2}}_{-\frac{1}{2}\frac{1}{2}}(\theta_{\Lambda(1520)}) d^{\frac{3}{2}}_{\frac{1}{2}\frac{1}{2}}(\theta'_p) e^{-i\phi_{\Lambda(1520)}} + H_2 e^{i\phi_{H_2}} d^{\frac{1}{2}}_{-\frac{1}{2}-\frac{1}{2}}(\theta_{\Lambda(1520)}) d^{\frac{3}{2}}_{-\frac{1}{2}\frac{1}{2}}(\theta'_p) e^{-i\phi'_p}$
$-\frac{1}{2}$	$-\frac{1}{2}$	$-(H_1 e^{i\phi_{H_1}} d^{\frac{1}{2}}_{-\frac{1}{2}\frac{1}{2}}(\theta_{\Lambda(1520)}) d^{\frac{3}{2}}_{\frac{1}{2}-\frac{1}{2}}(\theta'_p) e^{-i(\phi_{\Lambda(1520)}-\phi'_p)} + H_2 e^{i\phi_{H_2}} d^{\frac{1}{2}}_{-\frac{1}{2}-\frac{1}{2}}(\theta_{\Lambda(1520)}) d^{\frac{3}{2}}_{-\frac{1}{2}-\frac{1}{2}}(\theta'_p))$

Table 6
Amplitudes for nonresonant $\Lambda_c^+(\frac{1}{2}^+) \to pK^-\pi^+$ decay mode.

m	λ_p	Amplitude
$\frac{1}{2}$	$\frac{1}{2}$	$N_{++} e^{i\phi_{N++}}$
$\frac{1}{2}$	$-\frac{1}{2}$	$N_{+-} e^{i\phi_{N+-}}$
$-\frac{1}{2}$	$\frac{1}{2}$	$N_{-+} e^{i\phi_{N-+}}$
$-\frac{1}{2}$	$-\frac{1}{2}$	$N_{--} e^{i\phi_{N--}}$

3 Experiment E791 and Data Reduction

We analyze data from Fermilab fixed-target experiment E791, which ran from 1991–1992. The data were recorded from 500 GeV/c π^- beam interactions in five thin target foils (one platinum, four diamond) whose centers were separated by about 1.53 cm. The detector, described elsewhere in more detail[10,11], was a large-acceptance, forward, two-magnet spectrometer. Its key components for this study included eight planes of multiwire proportional chambers, and six planes of silicon microstrip detectors (SMD) before the target for beam tracking, a 17-plane SMD system and 35 drift chamber planes downstream of the target for track and vertex reconstruction, and two multicell threshold Čerenkov counters for charged particle identification.

An unrestrictive, open-charm event selection based on total transverse energy

seen in the calorimeters was made in real time. Then offline we require all Λ_c event candidates to have a production and decay vertex longitudinally separated by at least 6 σ_l, where σ_l is the error in that separation. The tracks and vertex fits satisfy χ^2 requirements. The vertex must be formed from proton, kaon, and pion tracks identified as such by the Čerenkov particle identification system. Proton candidates are rejected when projected into regions of the detector with poor particle identification efficiency. To reject more background, we require that the magnitude of the vector sum of the transverse momenta, p_t, of all the secondary tracks with respect to the flight path of the reconstructed Λ_c candidate be ≤ 0.4 GeV/c. In order to eliminate reflections from $D^+ \to K^-\pi^+\pi^+$ decays and from D^+, $D_s^+ \to K^-K^+\pi^+$ decays, we remove all events whose reconstructed $K\pi\pi$ mass is within the range [1.85, 1.89] GeV/c^2 or whose reconstructed $KK\pi$ mass is within either of the ranges [1.85, 1.89] GeV/c^2 or [1.95, 1.99] GeV/c^2.

After this preliminary stage of the analysis, we have 998±167 $\Lambda_c^+ \to pK^-\pi^+$ signal events and 107,368±366 background events. Therefore we apply further requirements in order to improve this signal in an unbiased way. This is accomplished by a selection on the output of an artificial neural network. The network is trained using a Monte Carlo (MC) sample of $\Lambda_c^+ \to pK^-\pi^+$ decays for signal and events from the wings of the $pK^-\pi^+$ mass distribution in data for background. The variables used in the training include all those described in the preliminary analysis above and the transverse miss distance between the primary vertex and the line of flight of the reconstructed Λ_c candidate, the scalar sum of all the p_t^2 of all the secondary tracks with respect to the flight path of the reconstructed Λ_c candidate, the separation of the secondary vertex from the closest target foil edge expressed in number of standard deviations, the calculated proper lifetime of the reconstructed Λ_c, the ratio of the distance of each decay tracks from the secondary vertex to its distance from the primary vertex, and the minimum and product of the three such ratios.

The cut on the neural net output is chosen to maximize $N_{S,MC}/\sqrt{N_{S,MC} + N_B}$ where $N_{S,MC}$ is the number of MC signal events (scaled to our data size) and N_B the number of background events. After the cut on the neural net output, 2271 real events in the $pK^-\pi^+$ mass range of [2.18, 2.38] GeV/c^2 survive, as seen in figure 2, which corresponds to 886±43 signal events (significance of 20.4σ) and 1384±49 background events.

4 Differential Decay Rate Fit

Once the final data set is established we constrain each reconstructed $pK\pi$ mass to the mass of the Λ_c. This forces all candidate events, whether in the signal peak or in the wings, to have the same decay phase space as that of the

E791 VERY PRELIMINARY

$\Lambda_c^+ \to p K^- \pi^+$

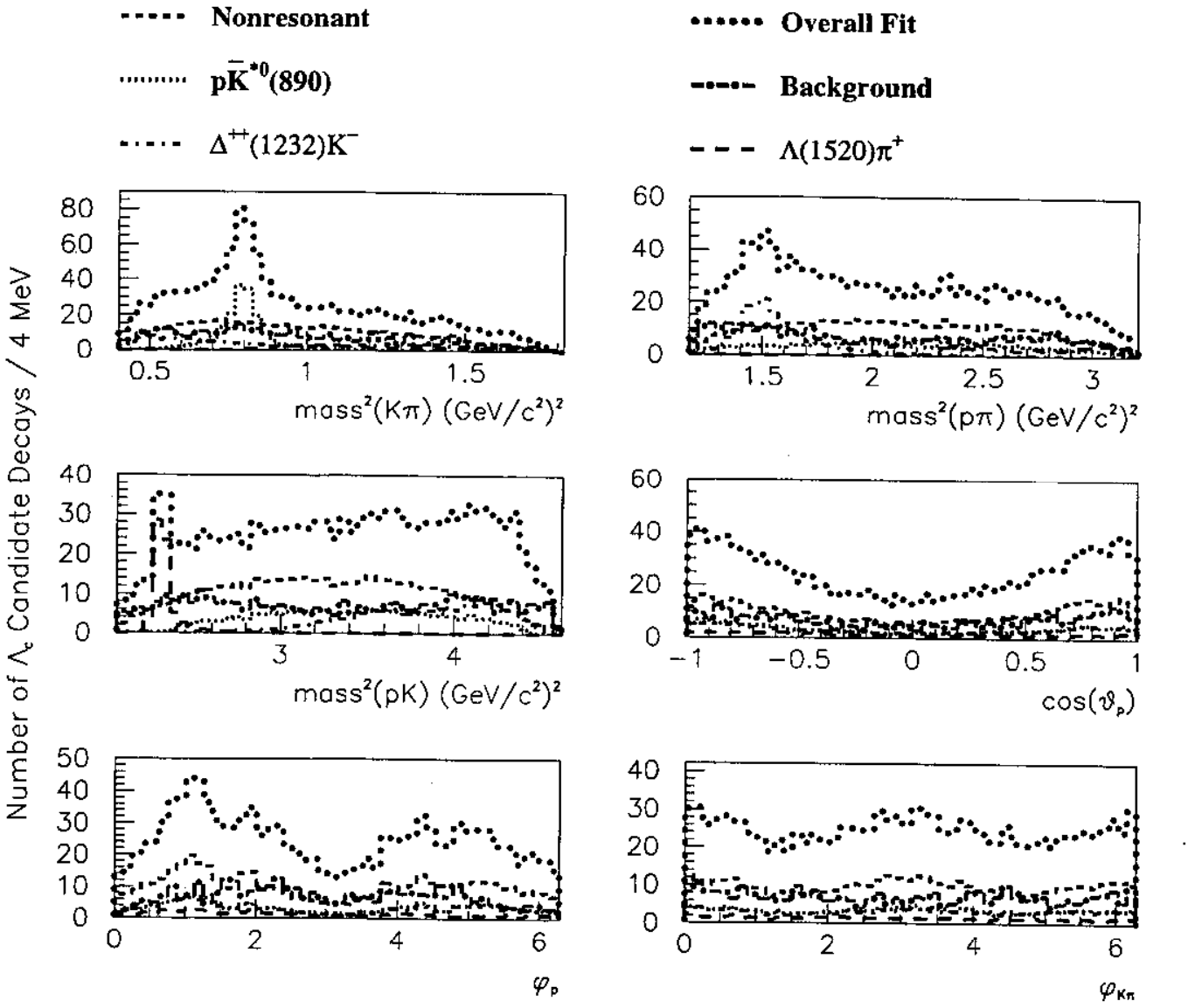

E791 VERY PRELIMINARY

$\Lambda_c^+ \to p K^- \pi^+$

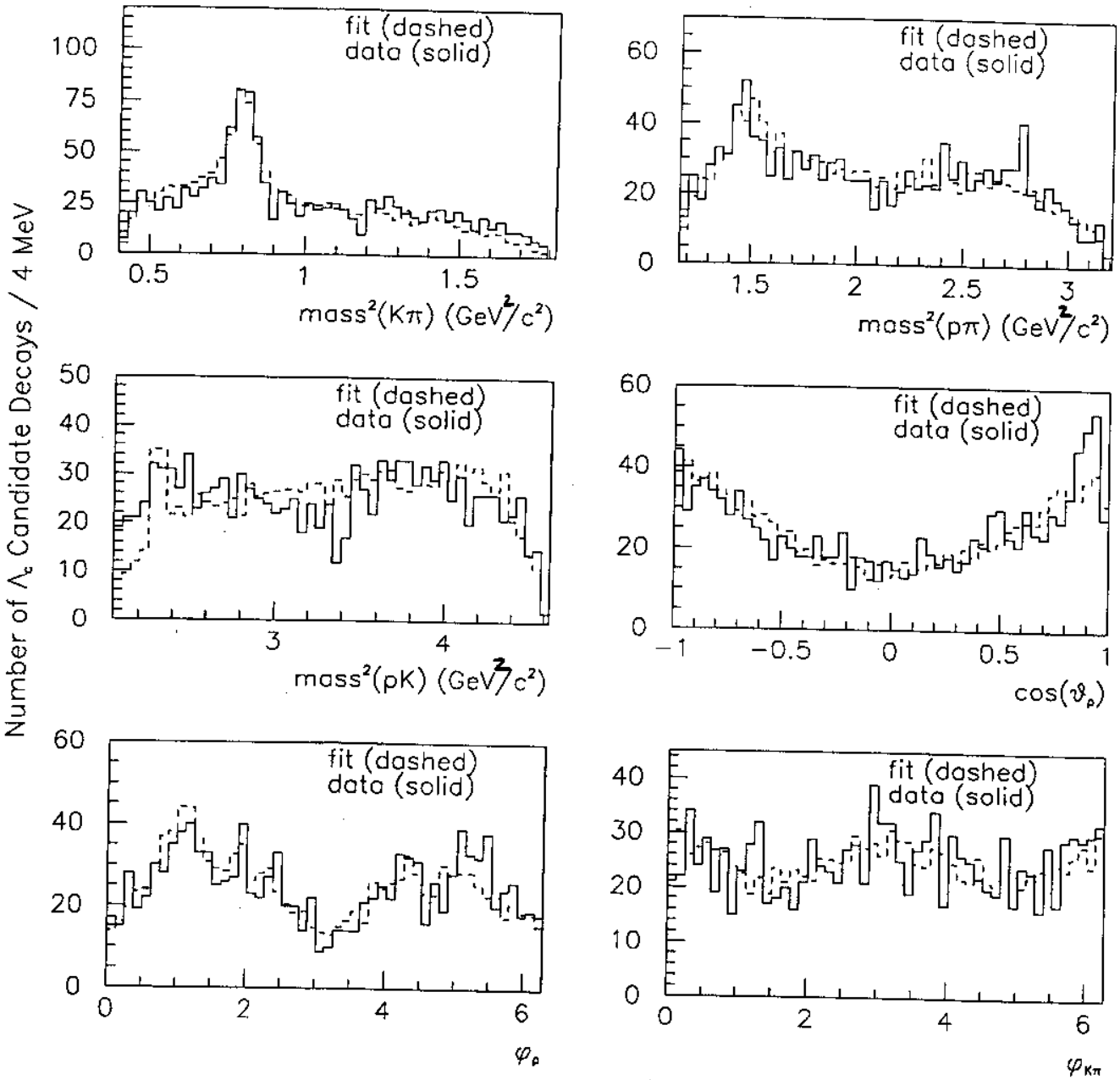

Additional resonances?

$\Lambda_c^+ \to \frac{1}{2}^- (\to p K^-)\ \pi^+$

$m = 1556 \pm 19$ MeV/c^2

$\Gamma = 279 \pm 74$ MeV/c^2

Also possible: Tail of $\Lambda(1405) \to p K^-$

E791 VERY PRELIMINARY

$\Lambda_c^+ \to pK^-\pi^+$

Table 6
The systematic errors on fit fractions.

Mode	Drift Chamber (%)	Čerenkov Counter (%)	Acceptance Adjust (%)	Production Model (%)	Combined Error (%)
$p\overline{K}^{*0}(890)$	1.7	0.6	0.3	0.0	1.8
$\Delta^{++}(1232)K^-$	2.5	1.2	0.7	0.1	2.9
$\Lambda(1520)\pi^+$	0.9	0.5	0.4	0.1	1.1
Nonresonant	3.2	1.1	0.9	0.1	3.5

Table 7
The decay fractions for $\Lambda_c^+ \to pK^-\pi^+$ with statistical and systematic errors from the final fit.

Mode	Fit Fraction (%)
$p\overline{K}^{*0}(890)$	19.5±2.6±1.8
$\Delta^{++}(1232)K^-$	18.0±2.9±2.9
$\Lambda(1520)\pi^+$	7.7±1.8±1.1
Nonresonant	54.8±5.5±3.5

FIT FRACTIONS

uncertainties are comparable because of our more general fit.

Table 8
Λ_c branching ratios relative to the inclusive $\Lambda_c^+ \to pK^-\pi^+$ branching fraction. The NA32 and ISR values were calculated from one-dimensional projections only.

Mode	E791	NA32[14]	ISR[15]
$p\overline{K}^{*0}(890)$	0.29±0.04±0.03	$0.35^{+0.06}_{-0.07}$±0.03	0.42±0.24
$\Delta^{++}(1232)K^-$	0.18±0.03±0.03	$0.12^{+0.04}_{-0.05}$±0.05	0.40±0.17
$\Lambda(1520)\pi$	0.15±0.04±0.02	$0.09^{+0.04}_{-0.03}$±0.02	
Nonresonant	0.55±0.06±0.04	$0.56^{+0.07}_{-0.09}$±0.05	

B.R.

5 Discussion and Conclusions

Significant resonant and non-resonant branching fractions are found in this analysis of a 20σ $\Lambda_c^+ \to pK^-\pi^+$ signal, the largest sample so far analyzed. The size of the sample allows for inclusion of relative phases of the various contributions and a full accounting of spin and production polarization for the first time in such an analysis. The $\Delta(1232)^{++}K^-$ and $\Lambda(1520)\pi^+$ decay modes are seen as statistically significant contributions for the first time, even when uncertainties associated with phases and other variables are included. The

E791 VERY PRELIMINARY

$\Lambda_c^+ \to p k^- \pi^+$

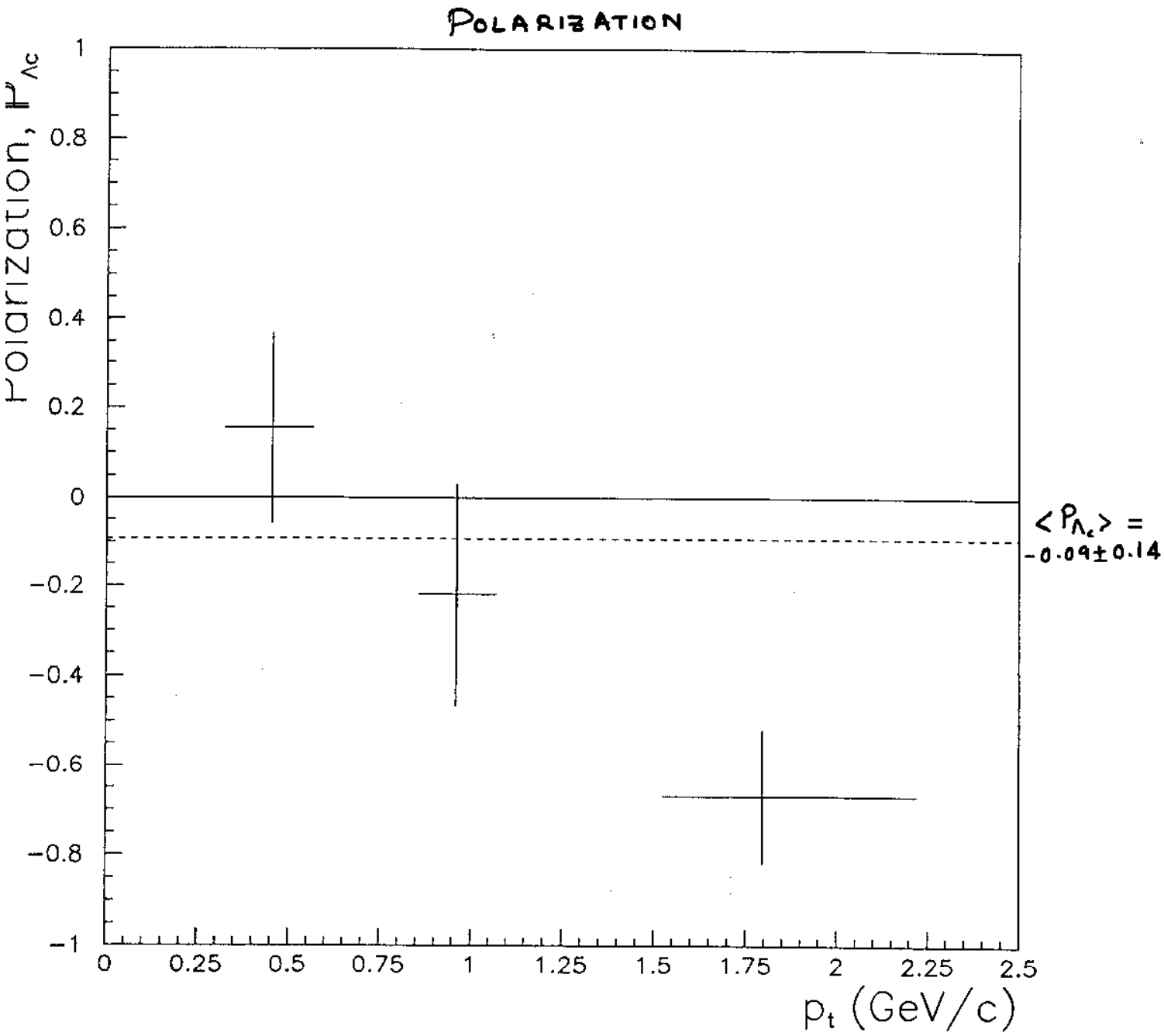

$0 < p_T < 0.71$ GeV/c

$0.71 < p_T < 1.24$ GeV/c

$1.24 < p_T < 5.20$ GeV/c

E791 VERY PRELIMINARY

$\Lambda_c^+ \to pK^-\pi^+$

Table 5
Decay amplitudes and polarization and mass plot parameters for $\Lambda_c \to pK\pi$ from the MINUIT fit with statistical errors.

FIT RESULTS

Terms	Parameter	Value
$p\bar{K}^{*0}(890)$	E_1	0.52± 0.17
	ϕ_{E_1}	-1.01± 0.48
	E_2	0.20± 0.10
	ϕ_{E_2}	2.35± 0.67
	E_3	0.21± 0.10
	ϕ_{E_3}	3.46± 0.42
	E_4	0.16± 0.10
	ϕ_{E_4}	5.29± 0.55
$\Delta^{++}(1232)K^-$	F_1	0.17± 0.07
	ϕ_{F_1}	4.98± 0.41
	F_2	0.38± 0.13
	ϕ_{F_2}	4.88± 0.40
$\Lambda^*(1520)\pi^+$	H_1	0.18± 0.09
	ϕ_{H_1}	5.93± 0.52
	H_2	0.20± 0.07
	ϕ_{H_2}	-0.06± 0.55
Nonresonant	N_{++}	0.46± 0.26
	$\phi_{N_{++}}$	3.48± 0.54
	N_{+-}	1.00
	$\phi_{N_{+-}}$	0.00
	N_{-+}	0.18± 0.15
	$\phi_{N_{-+}}$	0.75± 0.71
	N_{--}	0.94± 0.45
	$\phi_{N_{--}}$	1.13± 0.36
Polarization (bin 1)	$\mathbf{P}_{\Lambda_c,1}$	0.15± 0.21
Polarization (bin 2)	$\mathbf{P}_{\Lambda_c,2}$	-0.22± 0.25
Polarization (bin 3)	$\mathbf{P}_{\Lambda_c,3}$	-0.67± 0.15
# Signal Events	n_s	946± 38
# Background Events	n_b	1324± 43
Background Quad Term	b_q	-0.98± 10.51
Background Linear Term	b_l	1.34± 0.48
Mass_{Λ_c} (GeV/c^2)	m_0	2.29± 0.00
Width_{Λ_c} (MeV/c^2)	σ_l	20.1± 4.8
Width_{Λ_c} (MeV/c^2)	σ_c	9.3± 0.6

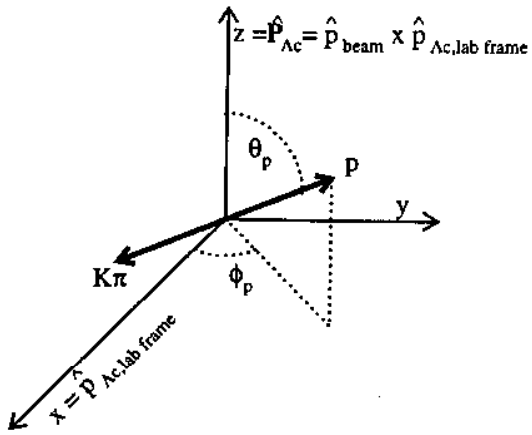
z = $\hat{P}_{\Lambda c}$ = $\hat{p}_{beam}$ x $\hat{p}_{\Lambda c,lab\ frame}$
θ_p
p
y
Kπ
ϕ_p
x = $\hat{p}_{\Lambda c,lab\ frame}$

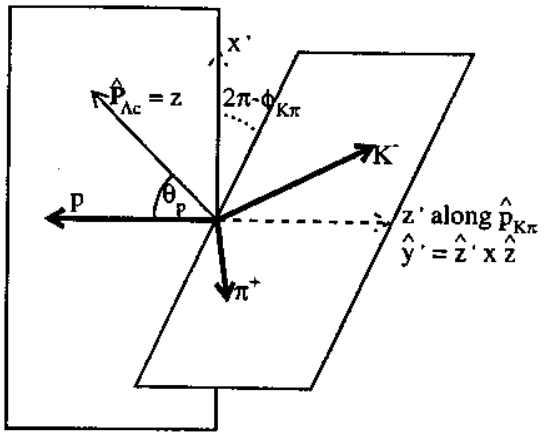
x'
$\hat{P}_{\Lambda c}$ = z
2π-$\phi_{K\pi}$
K$^-$
p
θ_p
z' along $\hat{p}_{K\pi}$
$\hat{y}' = \hat{z}' \times \hat{z}$
π^+

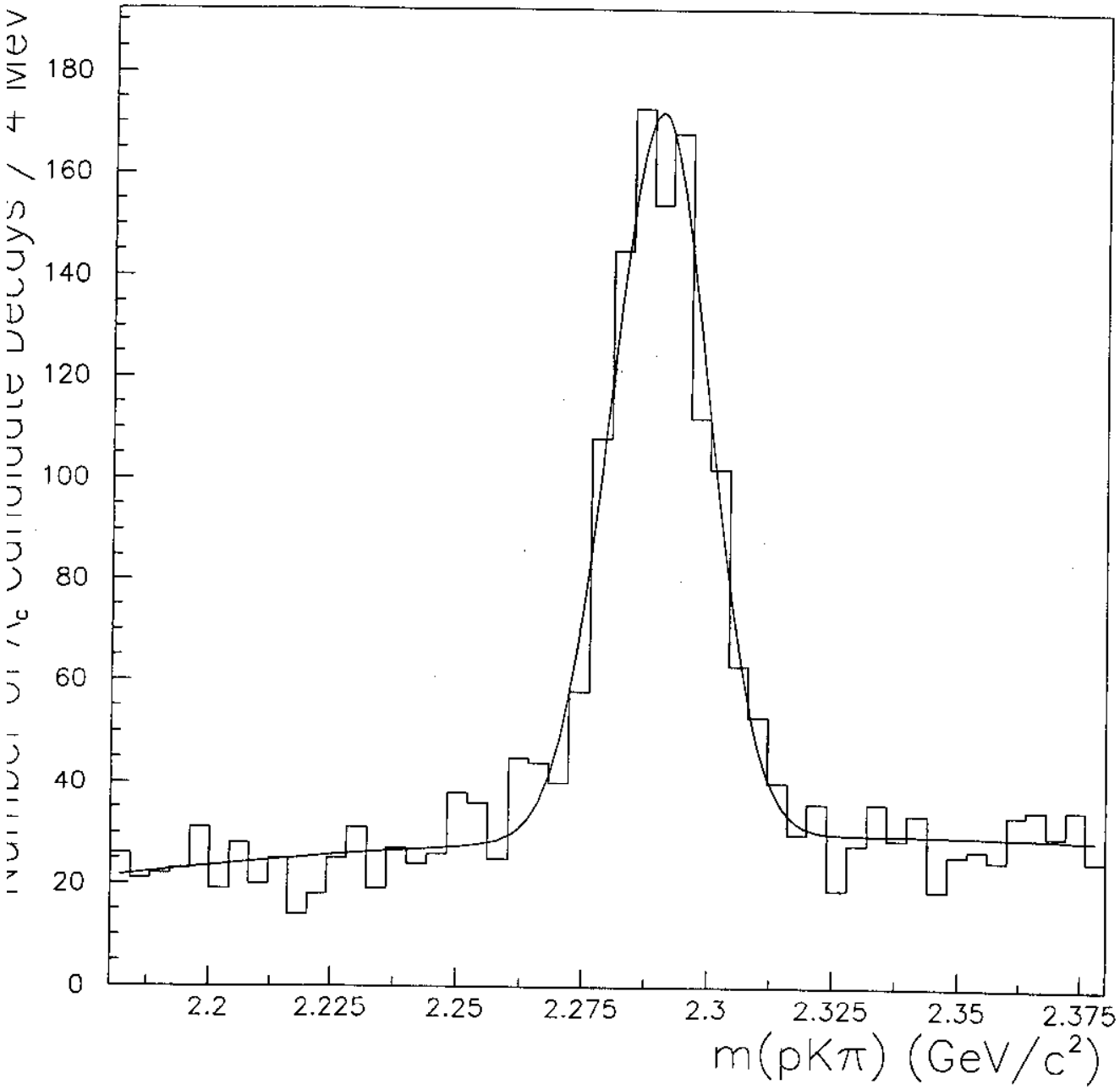
Number of Λc candidate decays / 4 MeV
180
160
140
120
100
80
60
40
20
0
2.2
2.225
2.25
2.275
2.3
2.325
2.35
2.375
m(pKπ) (GeV/c²)

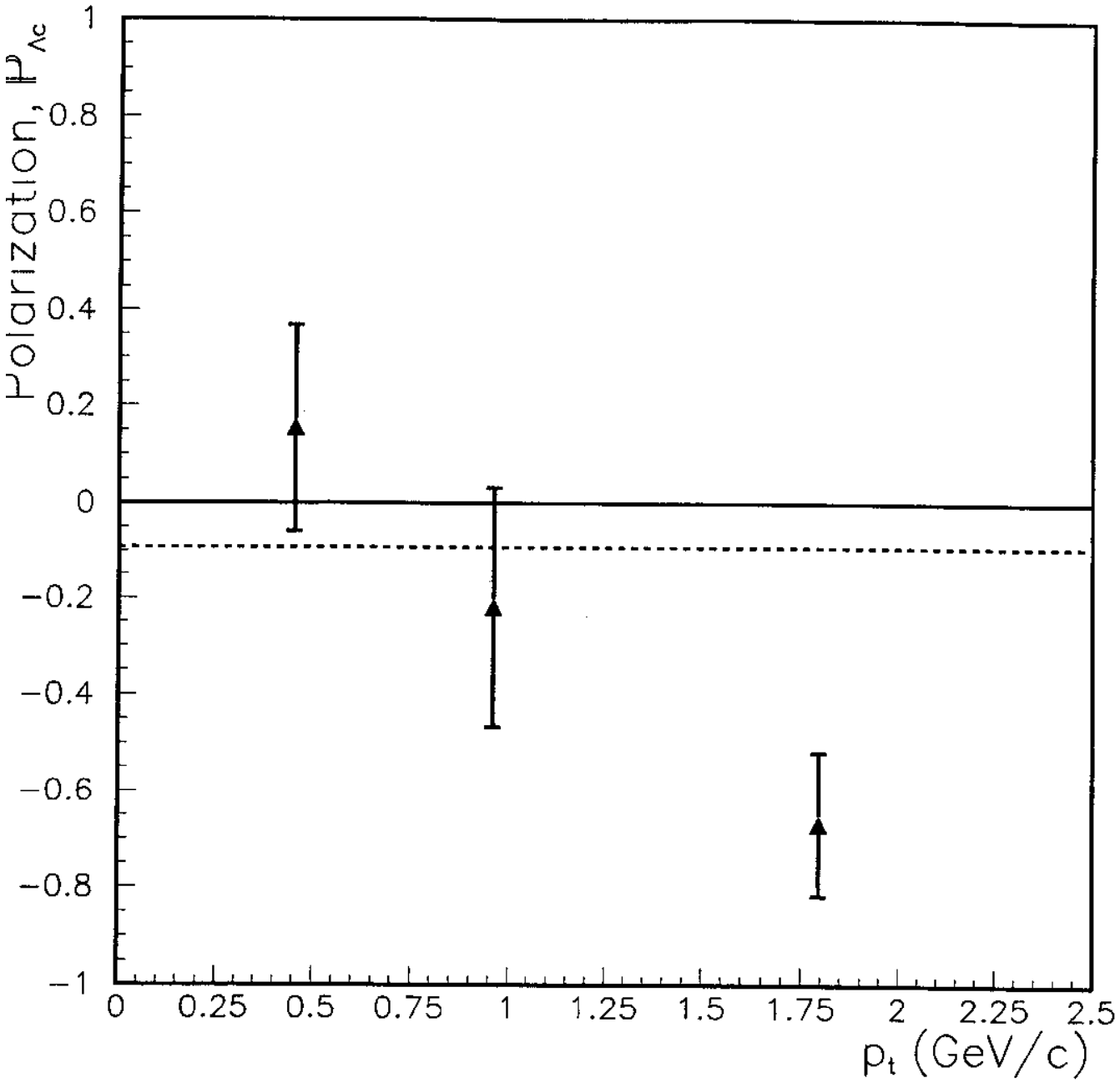
Polarization, $P_{\Lambda c}$
1
0.8
0.6
0.4
0.2
0
−0.2
−0.4
−0.6
−0.8
−1
0
0.25
0.5
0.75
1
1.25
1.5
1.75
2
2.25
2.5
p_t (GeV/c)

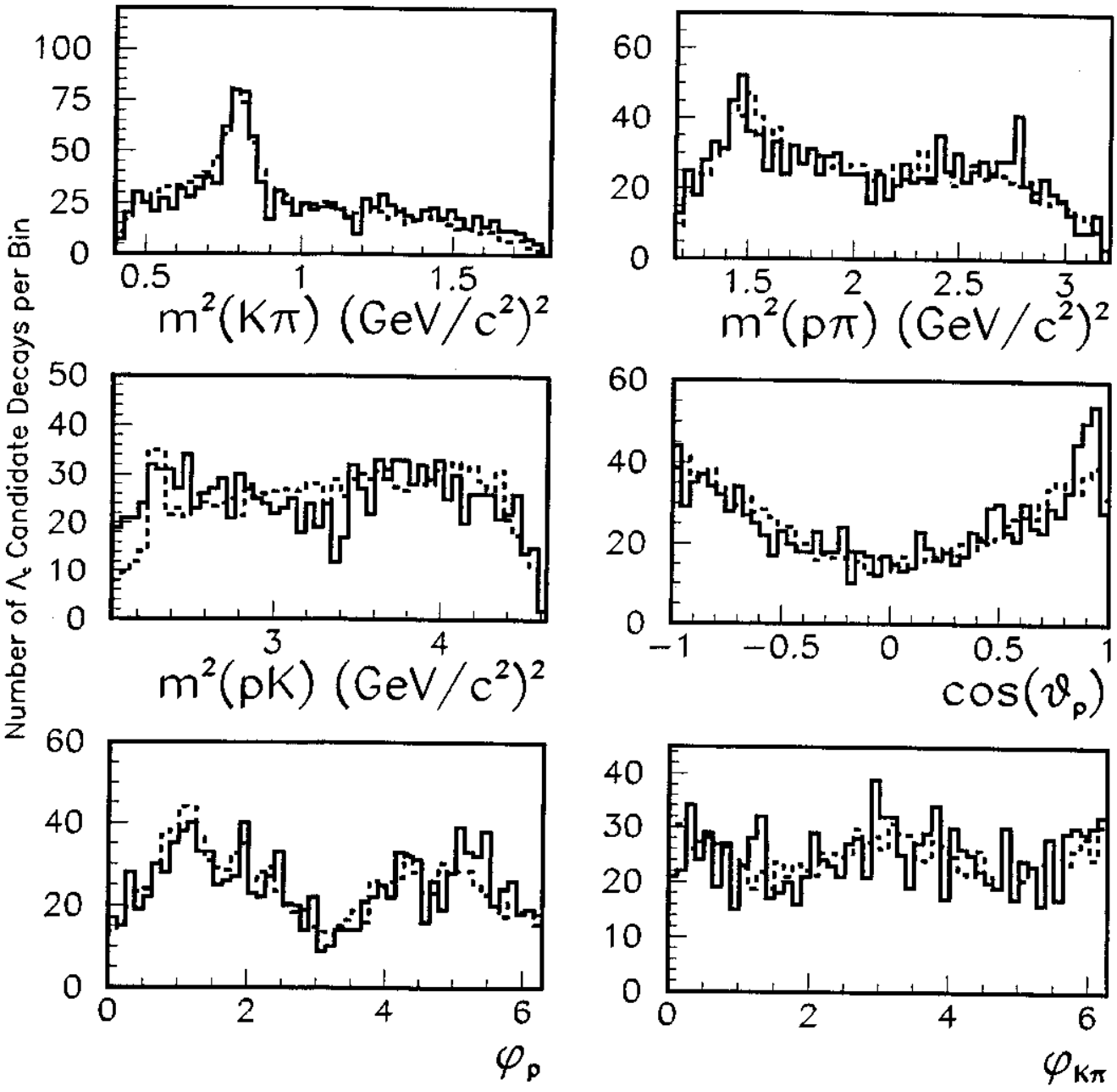
Number of Λ_c Candidate Decays per Bin
$m^2(K\pi)$ $(GeV/c^2)^2$
$m^2(p\pi)$ $(GeV/c^2)^2$
$m^2(pK)$ $(GeV/c^2)^2$
$\cos(\vartheta_p)$
φ_p
$\varphi_{K\pi}$

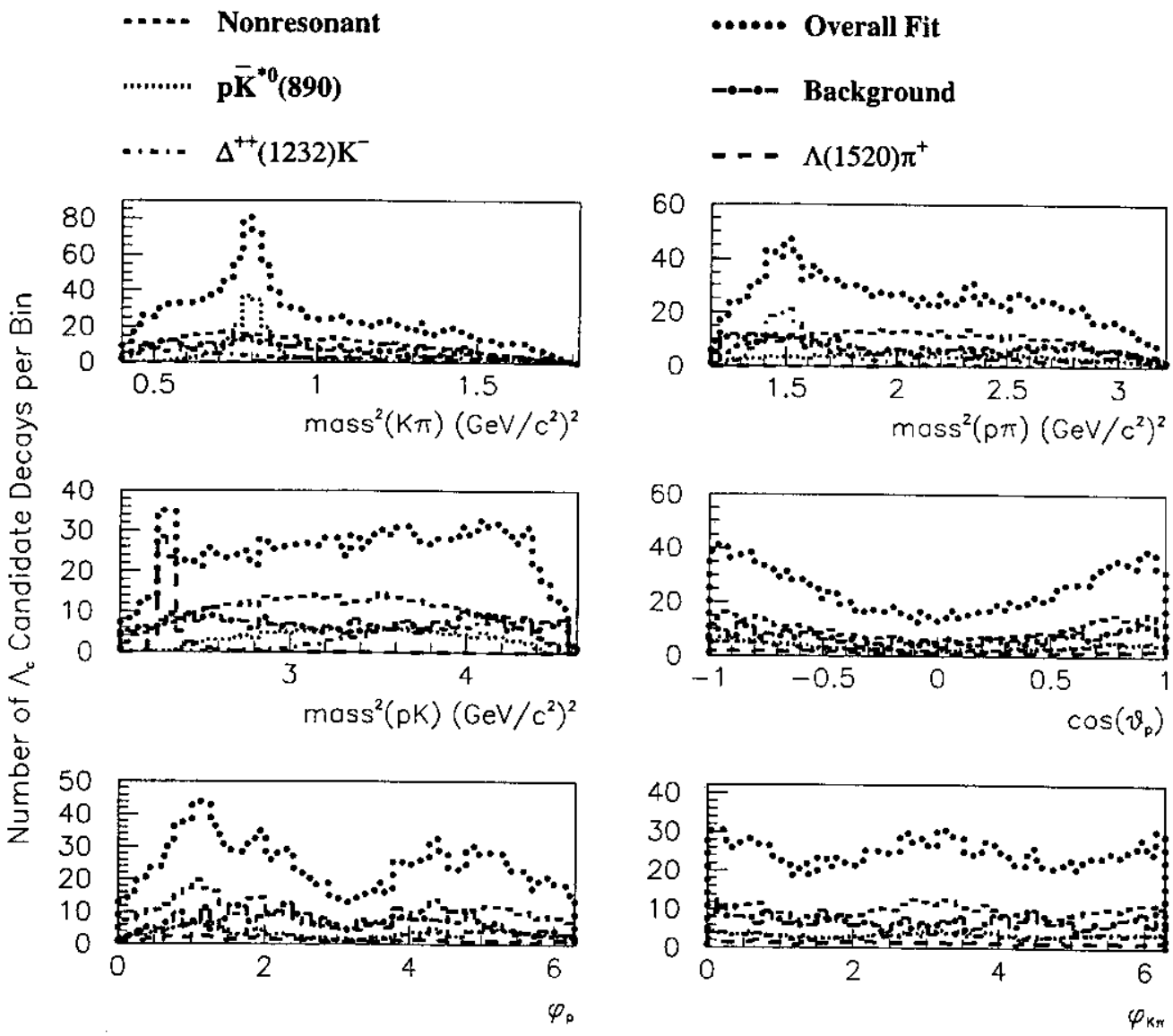
Nonresonant
Overall Fit
$p\bar{K}^{*0}(890)$
Background
$\Delta^{++}(1232)K^-$
$\Lambda(1520)\pi^+$
Number of Λ_c Candidate Decays per Bin
mass^2(Kπ) (GeV/c^2)^2
mass^2(pπ) (GeV/c^2)^2
mass^2(pK) (GeV/c^2)^2
cos(ϑ_p)
φ_p
$\varphi_{K\pi}$

Since the KSUSS applied a restriction that SDZ $\geq$ 6.0 and PTBAL $\leq$ 0.4 we also cut any events which violated these boundaries. See figures 6.2 and 6.3 for the real and MC data after the above cuts and reconstructed as pKπ, KKπ, and K$\pi\pi$.

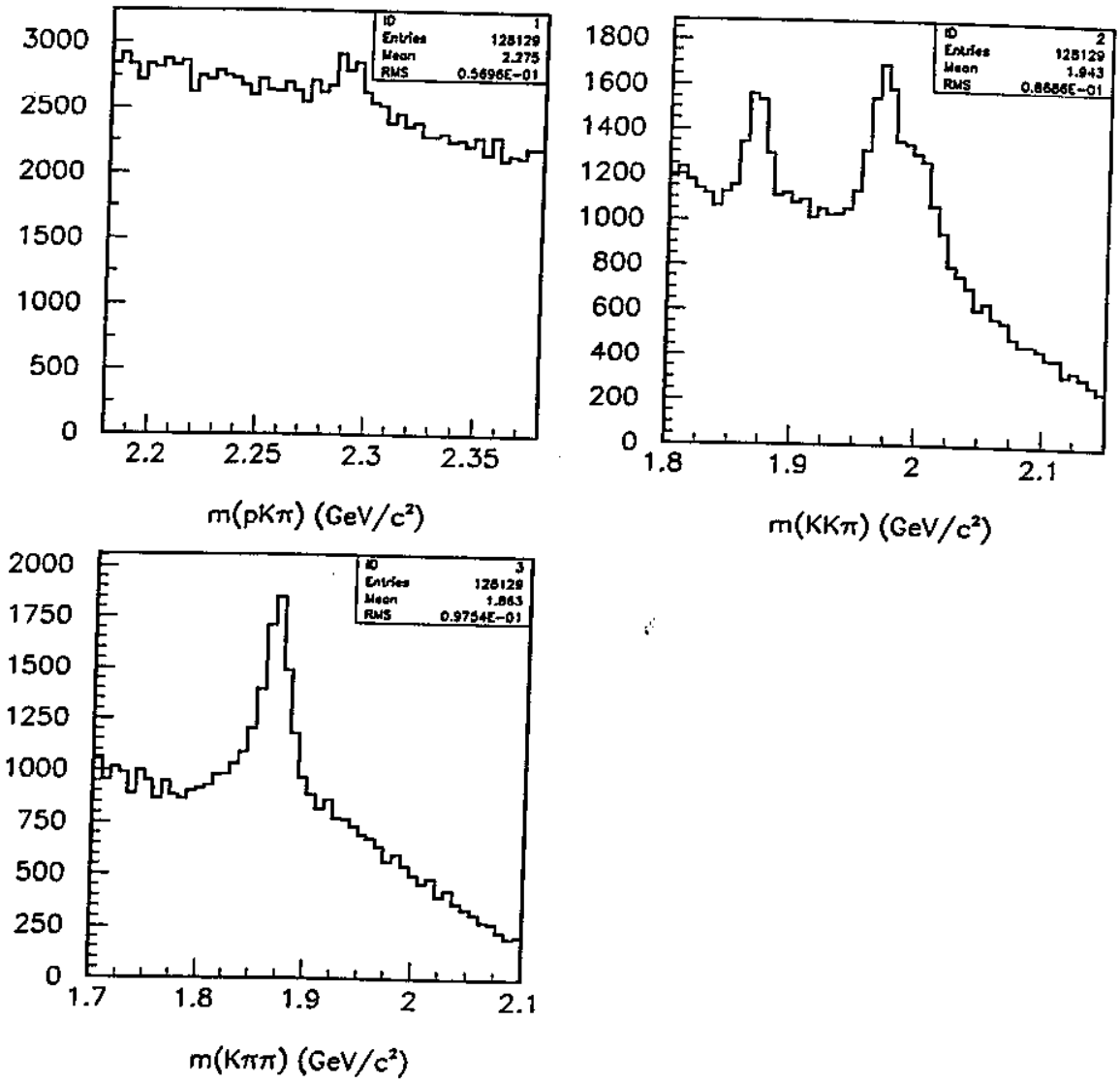

Figure 6.2: Reconstructed masses of real data before Neural Net and D mass cuts.

The last cut we made before using the Neural Net, was to eliminate the D resonances. There are three decays which are more likely to be reconstructed as false $\Lambda_c^+ \rightarrow pK^-\pi^+$ than other decays. They are

1. $D^+ \rightarrow K^+K^-\pi^+$
2. $D^+ \rightarrow K^-\pi^+\pi^+$
3. $D_s^+ \rightarrow K^+K^-\pi^+$

1384.1±48.8 background events and a significance of 20.4σ. See table 6.1 for detail on significance and alternate ways of calculating it.

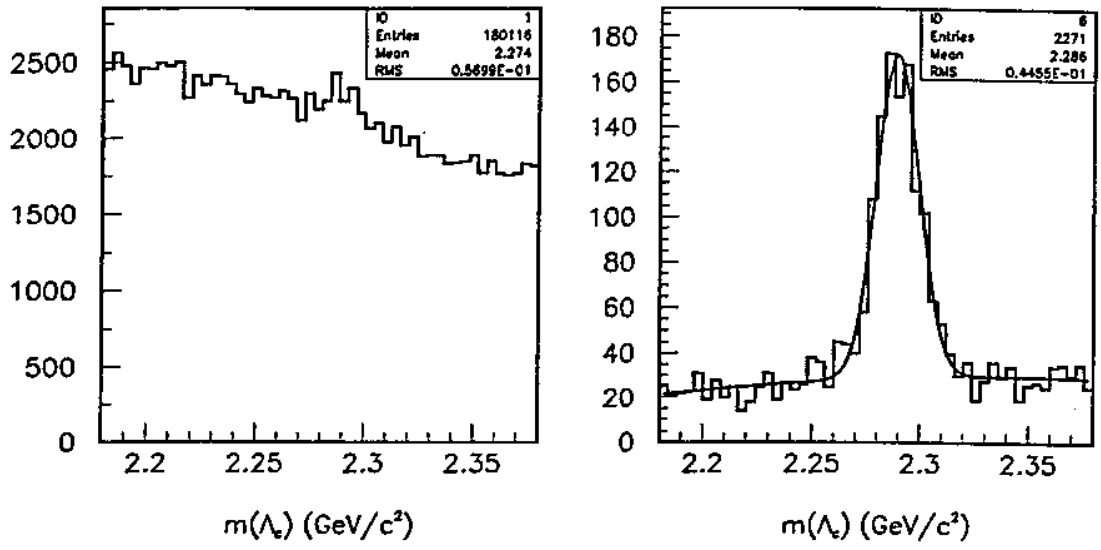

Figure 6.5: (left) Mass(pKπ) of the real data set before Neural Net cuts and (right) after. It has a significance of 20.4σ. There are 886±43 signal events and 1384 background events assuming that the peak is Gaussian, the background is quadratic and the number of signal and background events are variables.

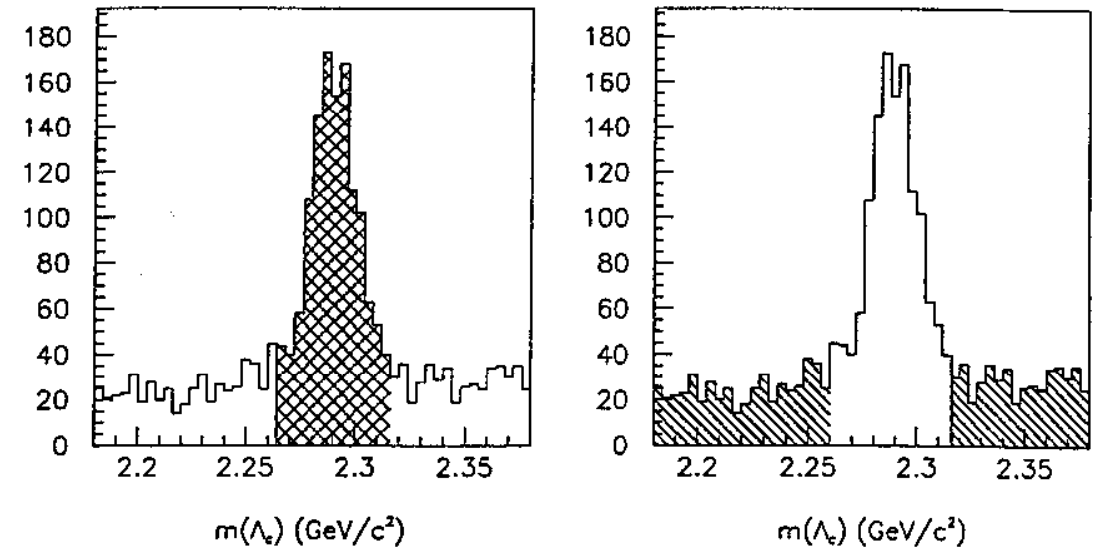

Figure 6.6: Mass(pKπ) of the real data set after the Neural Net cut. For future reference: the shaded area on the left refers to the signal region and on the right to the background regions.

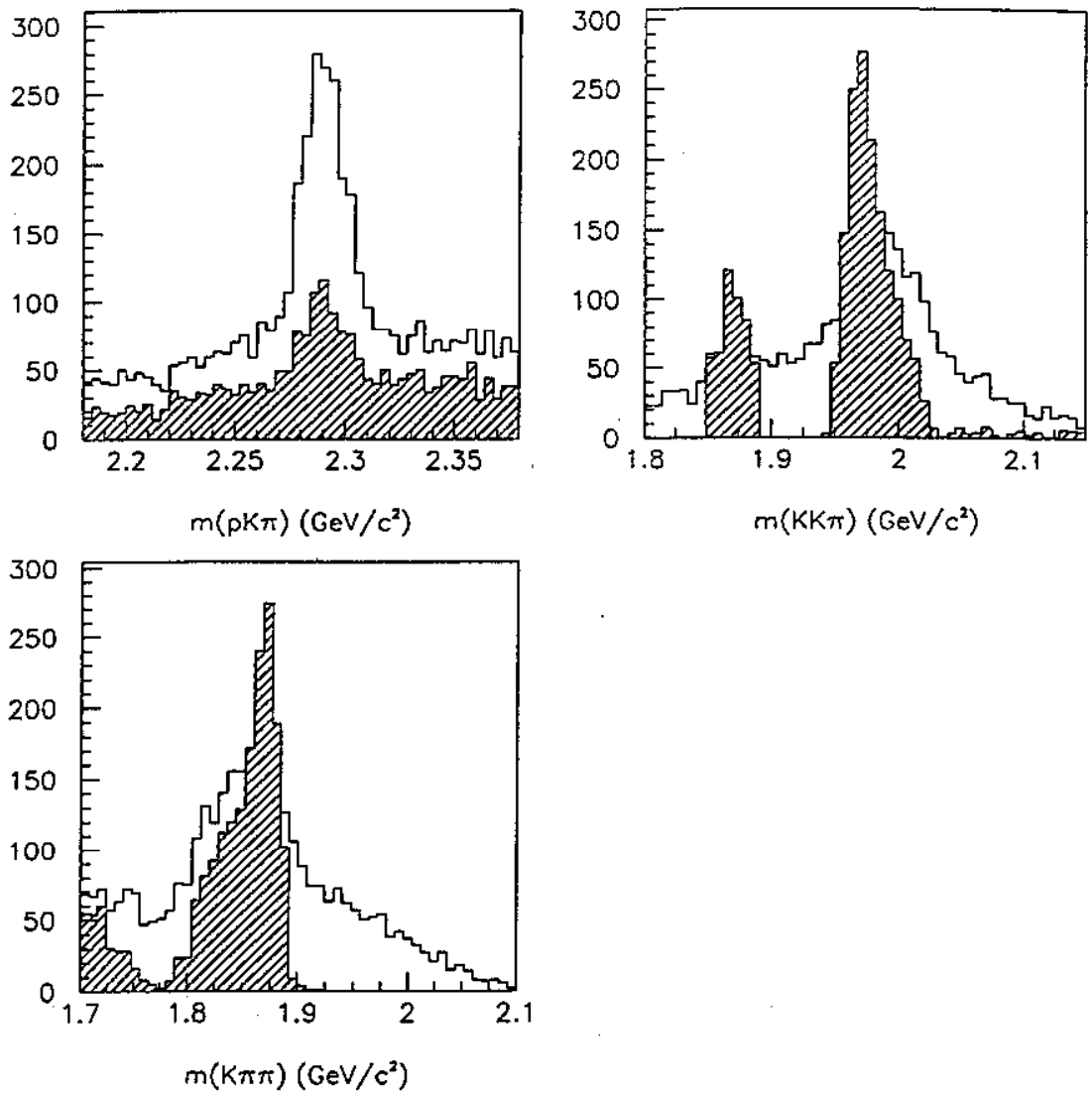

Figure 6.8: Reconstructed masses of real data after the Neural Net cuts are made. The shaded region is the region cut by the D mass cuts. This data set was produced by running the 19,763 events, which were in the D mass range and cut, through the Neural Net cut. The 2137 events of the 19,763 which survived are in the shaded region. These events are not used in the analysis. The larger outline is the total of the D region (2137 events) and the final data set (2271 events).

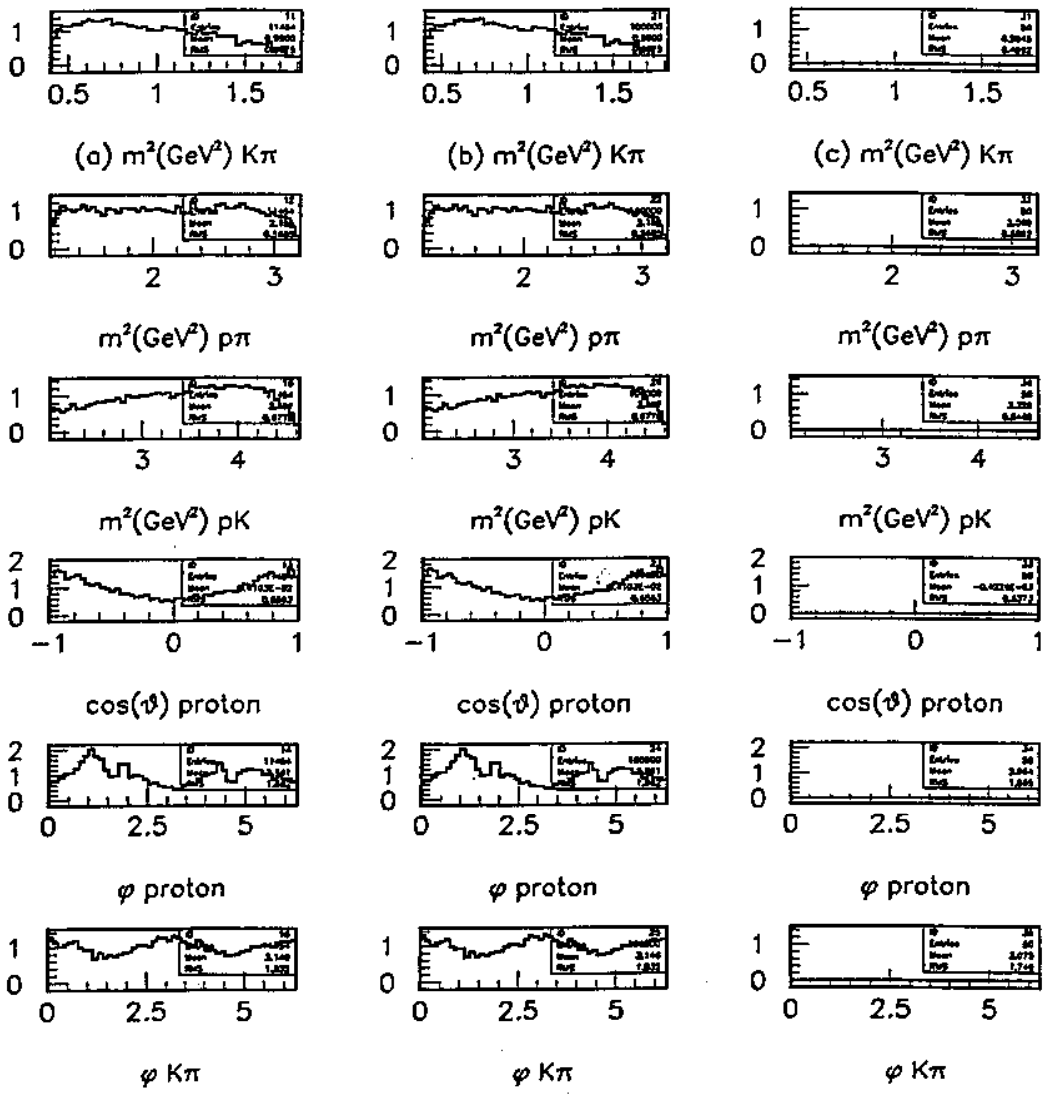

Figure 8.7: Acceptance. (a) The one dimensional projections of the surviving Monte Carlo divided by uniform phase space, (b) The model of the acceptance, (c) the difference between the real acceptance and the model.

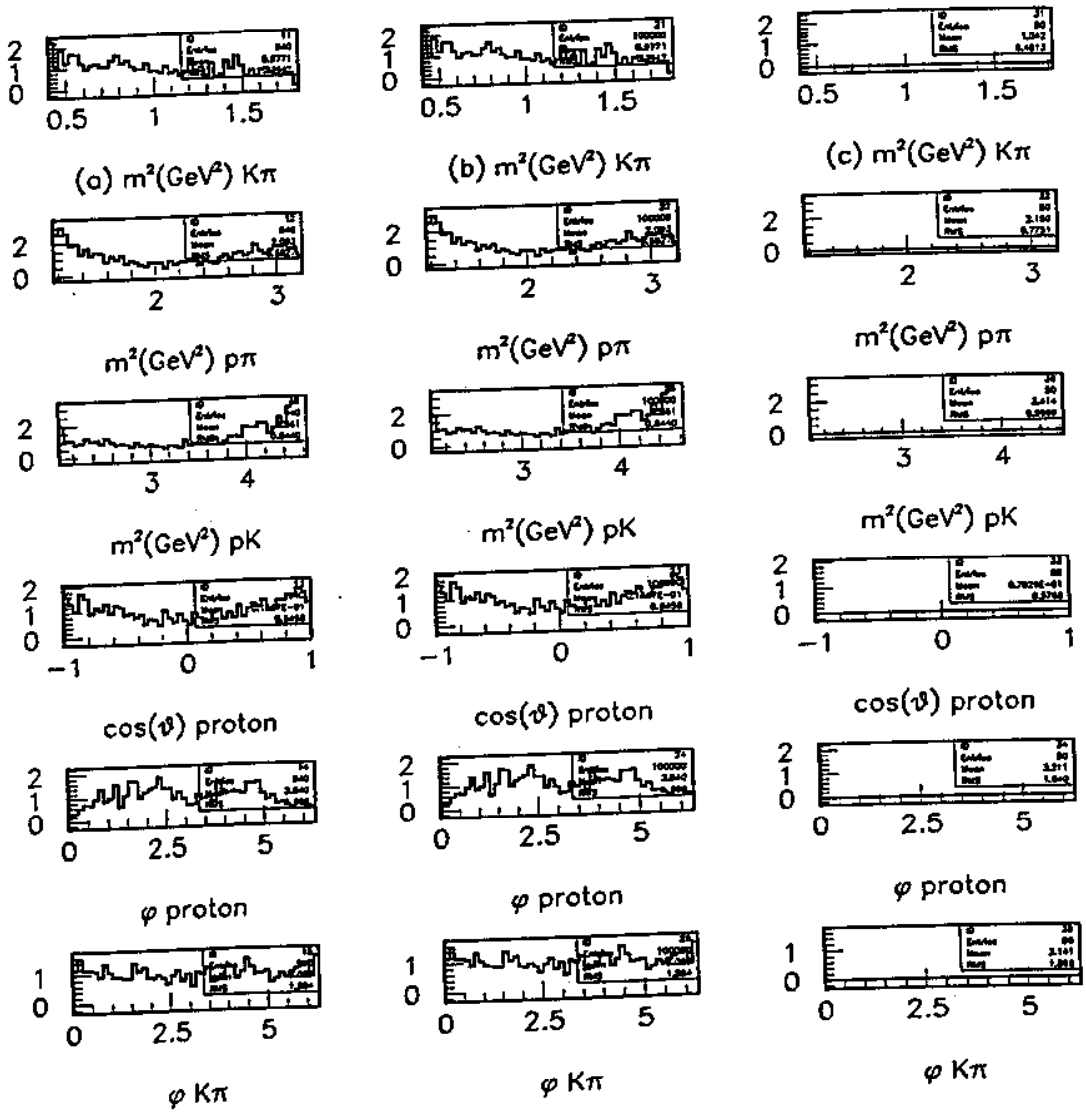

Figure 8.8: Background. (a) The one dimensional projections of the background divided by uniform phase space, (b) The model of the background, (c) the difference between the real background and the model.

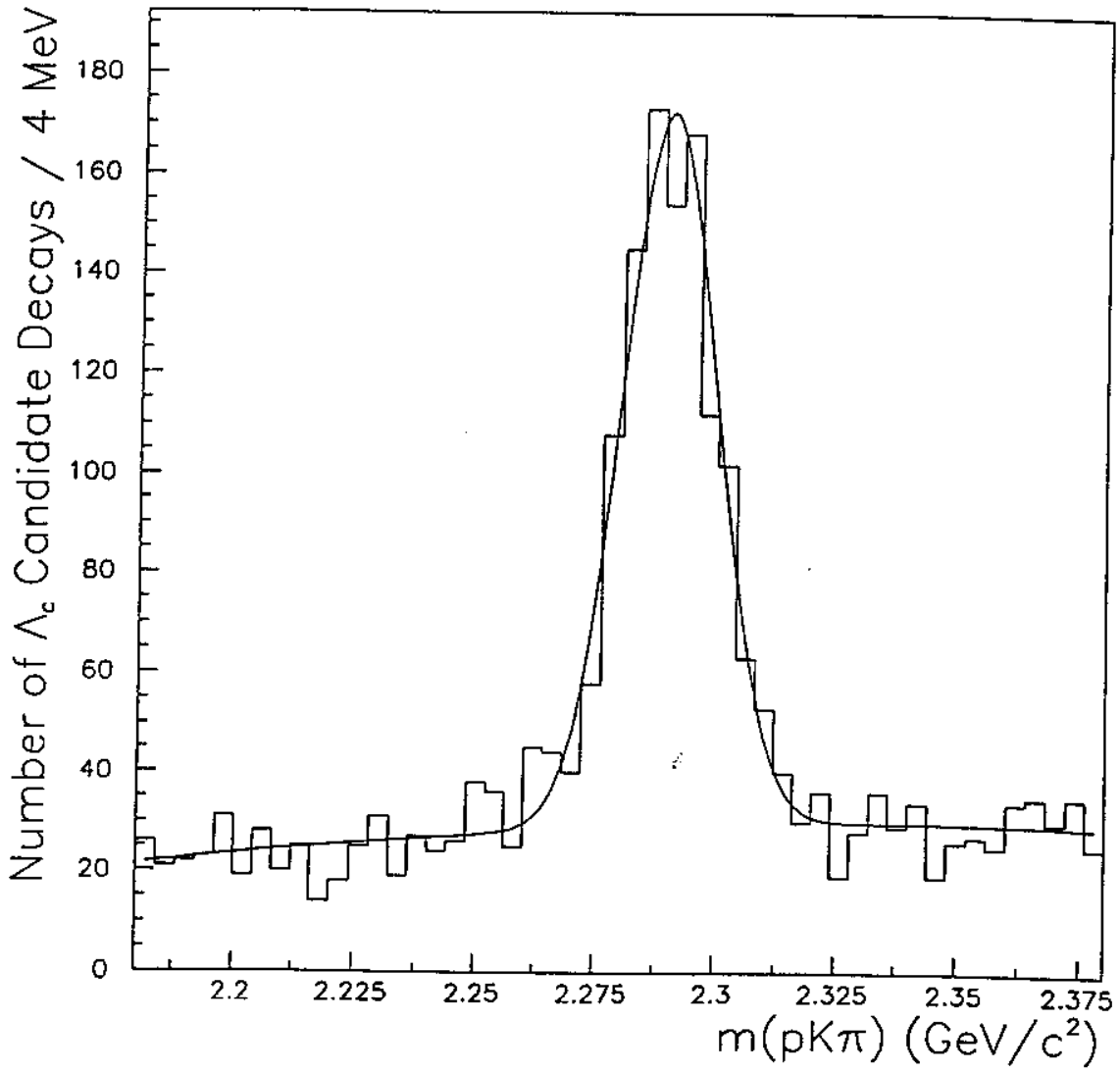

Figure 9.7: Mass(pKπ) of the real data set after Neural Net cuts and the MINUIT Fit 3. There are 946±38 signal events and 1324±43 background events assuming that the peak is Gaussian, the background is quadratic and the number of signal and background events are variables.

Mode	Fit 3p	Cerenkov(%)	Production(%)	DC hole(%)	2d Tweak(%)
$\overline{K}^{*0}$	19.5±2.6	18.9±2.7	19.5±2.7	21.2±3.0	19.8±2.8
Δ^{++}	18.0±2.9	16.8±2.8	18.1±2.9	20.5±3.3	17.3±2.9
$\Lambda(1520)$	7.7±1.8	8.3±1.9	7.6±1.8	6.8±1.7	7.3±1.8
Nonresonant	54.8±5.5	55.9±5.8	54.9±5.7	51.6±6.5	55.7±5.8

Table 10.2: The fit fractions for the decay $\Lambda_c \rightarrow pK\pi$ from the MINUIT fit.

Mode	Ckv(%)	Prod(%)	DC hole(%)	2d Tweak(%)	Syst Error (%)
$p\overline{K}^{*0}$	-0.6	0.0	+1.7	+0.3	1.8
$\Delta^{++}K^{-}$	-1.2	+0.1	+2.5	-0.7	2.9
$\Lambda(1520)\pi^{+}$	+0.5	-0.1	+0.9	-0.4	1.1
Nonres	+1.1	+0.1	-3.2	+0.9	3.5

Table 10.3: Deviations from the fit 3p fit fractions for the Systematic Errors.

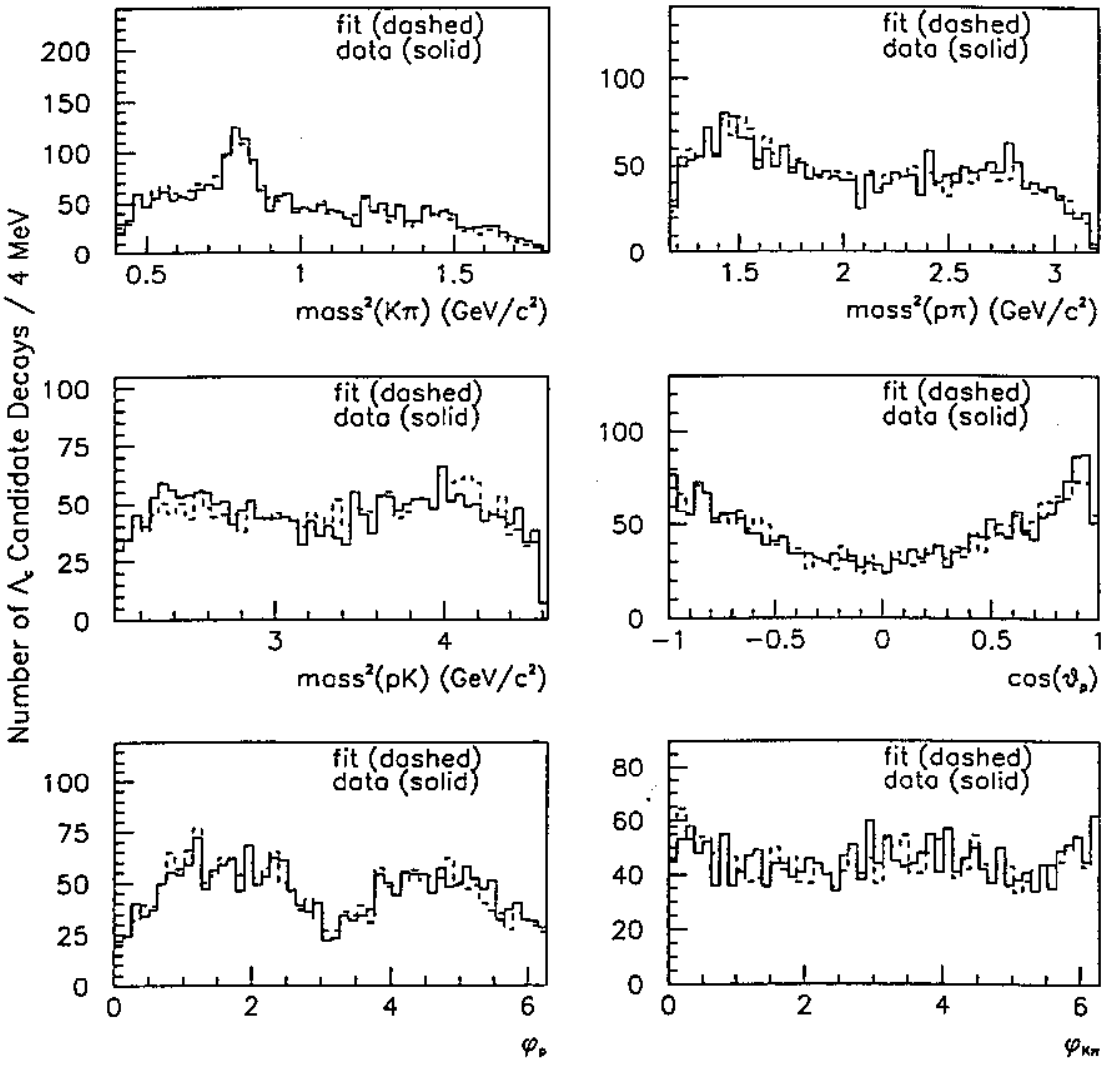

Figure K.1: The one dimensional projections of the new fit and real data.

CONCLUSIONS

- FULL 5-DIMENSIONAL ANALYSIS PERFORMED

- $\Lambda_c^+ \rightarrow$

$pK^-\pi^+$ (NR)	54.8	$\pm 5.5 \pm 3.5$ %
$p\bar{K}^{*0}$	19.5	$\pm 2.6 \pm 1.8$ %
$\Delta^{++}K^-$	18.0	$\pm 2.9 \pm 2.9$ %
$\Lambda(1520)\pi^+$	7.7	$\pm 1.8 \pm 1.1$ %

- AVERAGE Λ_c polarization is small
  but as a function of p_T gets up to $\sim -65\%$